Direct determination of state-to-state rotational energy transfer rate constants via a Raman-Raman double resonance technique: *ortho*-acetylene in $v_2=1$ at 155 K

José L. Doménech,[a] Raúl Z. Martínez, Ángel Ramos,[b] and Dionisio Bermejo
Instituto de Estructura de la Materia (CSIC), Serrano 123, E-28006 Madrid, Spain

(Received 23 December 2009; accepted 4 March 2010; published online 15 April 2010)

A new technique for the direct determination of state-to-state rotational energy transfer rate constants in the gas phase is presented. It is based on two sequential stimulated Raman processes: the first one prepares the sample in a single rotational state of an excited vibrational level, and the second one, using the high resolution *quasi*-continuous stimulated Raman-loss technique, monitors the transfer of population to other rotational states of the same vibrational level as a function of the delay between the pump and the probe stages. The technique is applied to the odd-*J* rotational states of $v_2=1$ acetylene at 155 K. The experimental layout, data acquisition, retrieval procedures, and numerical treatment are described. The quantity and quality of the data are high enough to allow a direct determination of the state-to-state rate constant matrix from a fit of the experimental data, with the only conditions of detailed balance and of a closed number of states. The matrix obtained from this direct fit is also compared with those obtained using some common fitting and scaling laws. © *2010 American Institute of Physics*. [doi:10.1063/1.3374031]

I. INTRODUCTION

Rotational energy transfer (RET) by collisions between gas phase molecules is a subject of interest in many areas of research, like energy balance in astrophysical media,[1] pressure broadening and line mixing of spectral lines,[2] or the chemistry of the Earth's atmosphere.[3] RET is also interesting from a more theoretical point of view since intramolecular potential energy surfaces are often tested by checking their ability to reproduce the state-to-state RET rates or cross sections,[4] or the closely related pressure broadening coefficients.

Early experimental studies of RET were based on the measurement of bulk properties of gases,[5] such as sound absorption or dispersion, which provide no state-resolved information. Pressure broadening coefficients measured over broad ranges of rotational states also provide information on the RET rates, but usually the number of unknowns (the state-to-state rate constants) is much higher than the number of experimental data available, and it is necessary to resort to fitting or scaling laws to reduce the number of parameters in the fits.[2] Recently, mapping of rotational population distributions in supersonic expansions[6] has also been proven to be a valuable tool to obtain the rate constants at low temperatures.

The development of tunable monochromatic lasers over the years has facilitated the growth of techniques based on monitoring the evolution of rotational populations by pump-probe time resolved experiments, providing a very direct path to obtain the state-to-state rate constants.[7] In these techniques, the pump process prepares the sample in a well defined initial rotational state, while the probe stage monitors the evolution of the population to other rotational states as a function of the delay (i.e., the number of collisions) between the pump and the probe. Several techniques have been used to prepare the state-selected sample, the most relevant being direct absorption of laser radiation,[8–13] the stimulated Raman effect[14–17] and stimulated emission pumping.[18] The literature shows many combinations of these pump methods with a variety of probe techniques: transient IR absorption,[8,9,13] laser-induced UV[14,19] or IR[8,9] fluorescence (LIF), resonant enhanced multiphoton ionization (REMPI),[17,15] coherent anti-Stokes Raman scattering (CARS),[20] etc.

In this paper, we present a new pump-probe technique based on the use of two sequential stimulated Raman scattering (SRS) processes, which we have applied to the $^{12}C_2H_2$ acetylene isotopologue. We have chosen for this study the subset of odd-*J* states. Since rotational state-changing collisions cannot induce a change of an odd number of rotational quanta due to nuclear spin-symmetry restrictions, we can consider this subset of states a closed system. In the first SRS process, two pulsed lasers promote population from the vibrational ground state of acetylene to a single rotational state of the $v_2=1$ vibrational level (one quantum of excitation on the symmetric C≡C stretch at 1974 cm^{-1}) through a Q-branch transition of the ν_2 band. After a controlled time delay, the second SRS process, this time using the *quasi*-continuous (q-cw) variant,[21] monitors the population that collisions have transferred to the different odd-*J* levels in $v_2=1$ by monitoring the intensity of the Q-branch lines of the $(v_2=2\leftarrow v_2=1)$ transition (i.e., the first hot band of ν_2 at 1959 cm^{-1}). To our knowledge, q-cw SRS has not been previously used as a probe technique in pump-probe experiments. Although it has less sensitivity than some of the abovementioned ones (REMPI, LIF, etc.), it has the advan-

[a]Author to whom correspondence should be addressed. Electronic mail: jl.domenech@iem.cfmac.csic.es.
[b]Present address: Laboratorio Nacional de Fusión (CIEMAT), Avda. Complutense 22, E-28040 Madrid, Spain.

tage of high spectral resolution and a very direct and linear relationship between the observed signals and the population of the levels involved.

As close antecedent to this work, we must mention that of Dopheide *et al.*,[14] where they study RET in $v_2=1$ of C_2H_2 at room temperature with stimulated Raman pumping and LIF probing. Orr[22] compiled an exhaustive review of many other energy transfer studies in acetylene, although the emphasis of these falls mostly on vibrational energy transfer paths.

II. BACKGROUND AND STRATEGY

The rotational state-to-state rate constants studied in this work are the kinetic rate constants of the process

$$C_2H_2(v_2=1,\ J=J_i)+M \rightarrow C_2H_2(v_2=1,\ J=J_f)+M+\Delta E_{\mathrm{kin}}, \tag{1}$$

i.e., after a collision, an acetylene molecule prepared in an initial state with one quantum of vibrational excitation and in a well defined rotational state J_i transfers or gains rotational energy to/from a collision partner M and ends up in a different rotational state J_f of the same vibrational state. ΔE_{kin} represents a possible change in the kinetic energy of the colliding pair after the collision. The probability of this rotational energy change happening is given by the (velocity-dependent) integral state-to-state cross section $\sigma_{f\leftarrow i}$. (We purposefully drop the J symbol in subindices for clarity.) The magnitudes that we want to obtain are the thermal state-to-state rate constants that are the average of $\sigma_{f\leftarrow i}$ over the relative velocity (v) distribution of the colliders, so $k_{f\leftarrow i}(T)=\langle v\sigma_{f\leftarrow i}\rangle=\int f(v)v\sigma_{f\leftarrow i}dv$. For a Maxwellian distribution at the center of mass system $f(v)=(\mu/2\pi k_BT)^{3/2}\times\exp(-\mu v^2/2k_BT)$ (where μ is the reduced mass of the colliding pair, k_B is the Boltzmann constant, and T is the temperature).[23] In this work, we study self-collisions in acetylene, thus the collider M has internal degrees of freedom that can also change upon a collision. The constants $k_{f\leftarrow i}$ that we are referring to are therefore sums over all possible final states and averages over all possible initial states of the acetylene molecule that acts as colliding partner.[24]

The change in population on each rotational state as collisions take place during a time interval dt (once the pump process is over and if there are no other relaxation mechanisms) can be described by

$$dN_f=\sum_{i\neq f}k_{f\leftarrow i}N_i dt-\sum_{i\neq f}k_{i\leftarrow f}N_f dt, \tag{2}$$

i.e., it is the balance between population added to that state (coming from the rest of accessible states) and population removed from that state (going to the rest of accessible states) by collisions. N_i and N_f are the time-dependent number densities of molecules in states i and f, respectively, if the $k_{f\leftarrow i}$ constants have L^3T^{-1} dimensions. We have chosen for $k_{f\leftarrow i}$ the units of pressure$^{-1}\times$time^{-1}, frequently found in the literature, and Eq. (2) can then be expressed as

$$dn_f(t)=\sum_{i\neq f}k_{f\leftarrow i}n_i(t)P dt-\sum_{i\neq f}k_{i\leftarrow f}n_f(t)P dt, \tag{3}$$

where n_i and n_f are the fractional populations of molecules in levels J_i and J_f, respectively, normalized to a total population of one. By denoting $k_{f\leftarrow f}\equiv-\Sigma_{i\neq f}k_{i\leftarrow f}$ (the negative of the total removal rate out of a given state f), the master equation (3) for a system with m levels can be written in the matrix form,

$$\begin{pmatrix} dn_1(t)\\ dn_2(t)\\ \vdots\\ dn_m(t)\end{pmatrix}=\begin{pmatrix} k_{1\leftarrow1} & k_{1\leftarrow2} & \cdots & k_{1\leftarrow m}\\ k_{2\leftarrow1} & k_{2\leftarrow2} & \cdots & k_{2\leftarrow m}\\ \vdots & \vdots & \ddots & \vdots\\ k_{m\leftarrow1} & k_{m\leftarrow2} & \cdots & k_{m\leftarrow m}\end{pmatrix}\begin{pmatrix} n_1(t)\\ n_2(t)\\ \vdots\\ n_m(t)\end{pmatrix}P dt \tag{4}$$

or, in a more compact form,

$$d\mathbf{n}(t)=\mathbf{k}\mathbf{n}(t)P dt. \tag{5}$$

The system of linear differential equations (4,5), has an analytical solution that can be expressed in terms of the eigenvalues and eigenvectors of the $\mathbf{k}$ matrix,[25]

$$\begin{pmatrix} n_1(t)\\ n_2(t)\\ \vdots\\ n_m(t)\end{pmatrix}=\begin{pmatrix} E_1^1 & E_1^2 & \cdots & E_1^m\\ E_2^1 & E_2^2 & \cdots & E_2^m\\ \vdots & \vdots & \ddots & \vdots\\ E_m^1 & E_m^2 & \cdots & E_m^m\end{pmatrix}\times\begin{pmatrix} e^{S_1Pt} & 0 & \cdots & 0\\ 0 & e^{S_2Pt} & \cdots & 0\\ \vdots & \vdots & \ddots & \vdots\\ 0 & 0 & \cdots & e^{S_mPt}\end{pmatrix}\begin{pmatrix} C_1\\ C_2\\ \vdots\\ C_m\end{pmatrix} \tag{6}$$

or, in a more compact form,

$$\mathbf{n}(t)=\mathbf{E}\exp(\mathbf{S}Pt)\mathbf{C}, \tag{7}$$

where the columns of the $\mathbf{E}$ matrix are the eigenvectors of the rate constant matrix $\mathbf{k}$, S_i are the eigenvalues of $\mathbf{k}$, and C_i are the integration constants that require boundary conditions to be determined. These boundary conditions can be the measured population distributions at a given time, so there is a different $\mathbf{C}$ vector for each pumped J state.

In order to retrieve the $\mathbf{k}$ matrix, we populate each odd-J level of $v_2=1$ and measure for each one of them the population of all odd-J levels of $v_2=1$ (both the initially prepared one and all those that are populated by collisions) as a function of the number of collisions ($P\times t$). After this process is completed, we have a set of time-dependent populations (decay for the initially pumped level and growths for the rest of levels) for each pumped J. All these sets of data are fitted simultaneously to Eq. (6) since they only differ in the C_i integration constants, but must satisfy the same $\mathbf{k}$ matrix. We do not impose any law on the rate constants, other than the sum rule

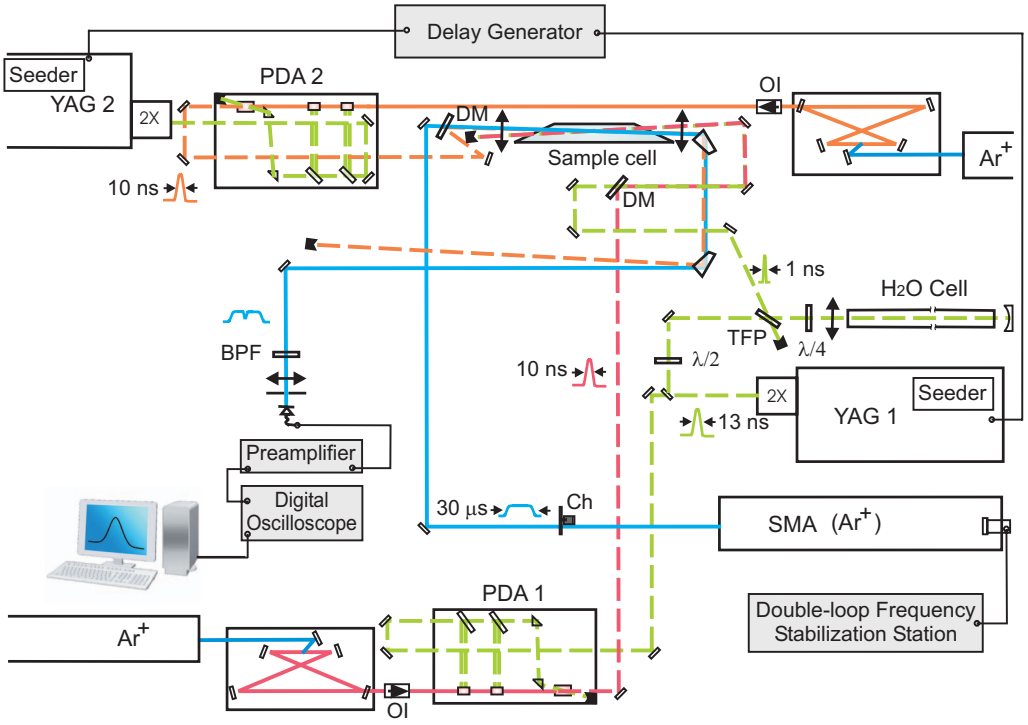

FIG. 1. Overview of the experimental setup. DM: dichroic mirror. OI: optical isolator. TFP: thin film polarizer. λ/4: quarter-wave plate. λ/2: half-wave plate. Ch: chopper. BPF: bandpass filter. The abbreviations for the main lasers and amplifiers are detailed in the body of the experimental section.

$$k_{f\leftarrow f} = -\sum_{i\neq f} k_{i\leftarrow f}, \tag{8}$$

which entails that there is a closed number of levels among which the total population remains constant, and the detailed balance condition,

$$k_{f\leftarrow i} = k_{i\leftarrow f}\frac{(2J_i+1)}{(2J_f+1)}\exp\left[-\frac{E_i-E_f}{kT}\right], \tag{9}$$

which relates the rate constants for upward and downward transitions. This allows us to reduce the number of unknown rate constants in Eq. (6) from m^2 to $m(m-1)/2$.

For the above described procedure to be valid, some requirements are to be fulfilled: (1) the relative populations must be reliably extracted from experimental signal intensities; (2) other sources of signal decay not related to collisions (i.e., molecular diffusion out of the probe volume) must also be accounted for; (3) possible competing process depleting the population (i.e., vibrational relaxation) must be also accounted for; (4) the pumping process must be over at the shortest considered delay (thus obviating the need to model the complex oscillatory behavior of the populations while the pump fields are on); and (5) all time-dependent signals corresponding to the same pumped J must be recorded with the same pressure and optical alignment. All these issues will be addressed in Sec. III.

This master equation model [Eqs. (4)–(7)] can account for multiple collisions: it describes processes in which the population arriving to a given level comes not only from the initially pumped one but also from other levels that have been populated in previous collisions. However, it must be noted that, as the population distribution evolves to the one at rotational thermal equilibrium, the information on the dynamics of the state-to-state transfer blurs (or, in other words, the lower the $P\times t$ considered, the richer is the information content of the data.) This also translates into the fact that, at low collision number, each column of the **k** matrix (elements $k_{f\leftarrow J}$) is mostly determined by the set of measurements obtained when pumping population to that J state.

Other retrieval strategies can be found in the literature. For example, Dopheide, Cronrath, and Zacharias[14] assumed single-collision conditions in their experiments, in which the population by collisions increases linearly with the collision number and each $k_{f\leftarrow i}$ can be determined independently, i.e., $n_f(t)\approx k_{f\leftarrow i}Ptn_i(0)$. As will be shown in Sec. IV, given our experimental conditions, the evolution of populations departs from this behavior. Rohlfing, Chandler, and Parker,[26] in their study of RET in v=1 HCl, fitted all time-dependent signals simultaneously, but they assumed that there is an initial time where the entire population resides on the initially pumped level, while it is zero in all other levels. Since we have observed significant population transfer to other levels during the pump process, we cannot share this assumption either. Our procedure is more similar to that followed by Sitz and Farrow[15] in their study of RET in v=1 N_2, i.e., a simultaneous fit of all observations to the same **k** matrix with a measured initial population distribution.

III. EXPERIMENTAL DETAILS

A. Optical layout

The experimental setup is based on our double resonance Raman-Raman setup[27] with some modifications, and it is depicted in Fig. 1. Recall that the SRS process requires two laser fields (usually a fixed frequency one and a tunable one) whose frequency difference matches that of a Raman-

allowed transition of the sample. The two fields couple through the third-order nonlinear electric susceptibility of the medium (a photon is exchanged between the two fields) in a self-phase-matched process, while the internal energy change in the molecule closes the energy balance. In this work, we use two consecutive SRS processes: the first one to pump population to $v_2=1$, $J=J_i$, and the second one to probe the population redistributed by collisions to $v_2=1$, $J=J_f$. In this paper, we use the terms "pump pair of lasers" and "probe pair of lasers" for the lasers involved in the first and second processes, respectively.

1. The pump pair

The tunable laser field is the output of a three-stage pulsed dye amplifier (PDA) seeded by a single-mode ring dye laser and pumped by an injection-seeded, 10 Hz, Q-switched, Nd^{3+}:YAG (YAG denotes yttrium aluminum garnet) laser. The fixed-frequency laser field is a fraction of the same Nd^{3+}:YAG laser that is temporally compressed in a stimulated Brillouin cell.[28] From now on we refer to these lasers (or the signals that they produce in a photodiode) as YAG1 (pump stage Nd^{3+}:YAG), SBS (compressed YAG1 pulse by the stimulated Brillouin effect), and PDA1 (pump stage PDA, pumped by YAG1). The goal of compressing the YAG1 pulse in the Brillouin cell is to shorten the duration of the pump stage. The time scale in which rotational relaxation takes place under our experimental conditions is not much larger than the duration of the pulses, so during the pump process there is already a small but significant population relaxation. To minimize this relaxation before Eq. (4) starts to be a valid representation of the time evolution of the populations, the shortest pump pulses compatible with the necessary spectral resolution are desirable. Since the population pumping rate is proportional (among other factors such as the population difference) to the product of the irradiances of the pump lasers, compressing one of them is enough to shorten the pump process duration.

The stimulated Brillouin cell is a 2.3-m-long glass tube filled with microfiltered (200 nm pore size) water. The design follows that of Neshev and collaborators,[29] although no baffles are used in our setup. At the rear window of the cell, a 10 cm focal length concave mirror reflects YAG1 back into the water cell, forming a focus where the leading edge of the incoming pulse generates a stimulated Brillouin seed. This seed travels backward and is amplified by the rest of the incoming pulse that is, in turn, depleted. If the length of the scattering medium matches the length of the pump pulse, the SBS pulse emerges just as the tail of the incoming pulse has entered the medium, achieving a high degree of compression, in our setup, from ~3 ns down to ~1 ns full width half maximum (FWHM). The SBS reflection is phase conjugated and it travels back along the same path as the incident pulse, so polarization optics are used to separate them: a combination of a thin film polarizer (TFP) and a quarter-wave plate before the front window of the SBS cell form an optical isolator/splitter that allows a convenient separation of both beams. The reflected SBS pulse is both frequency downshifted and spectrally broadened with respect to the original YAG1 pulse. In order to spectrally characterize the SBS beam, we scanned the frequency difference in the pump pair across the Q(7) line of the ν_2 band, while we monitored the SRS signal when the frequency difference in the probe pair was held fixed at the center frequency of the Q(7) line of the $2\nu_2$-ν_2 band. This allowed us to measure a spectral width of 0.016 cm^{-1} (FWHM) and a frequency redshift of 0.250 cm^{-1} for the SBS beam, in agreement with the expected values from the literature.[30] Optical delays are introduced, by appropriately folding the beam paths so that the SBS and the PDA1 pulses overlap in time upon reaching the sample cell.

TABLE I. Characteristics of the four beams involved in the two stimulated Raman processes.

Laser beam	Energy per pulse or power	Pulse duration (ns FWHM)	Spectral width (MHz)
PDA1	10 mJ	13	40
SBS	15 mJ	1	533
PDA2	12 mJ	10	40
SMA	400 mW	N/A	1

2. The probe pair

The tunable laser field is the output of another PDA (herein PDA2) seeded by a second single-mode ring dye laser and pumped by a second injection-seeded, Q-switched, Nd^{3+}:YAG laser (herein YAG2) with a repetition rate of 30 Hz. The fixed-frequency laser field is a cw single-mode Ar^+ laser (herein the SMA laser) operating at 529 nm, frequency locked to a sub-Doppler transition of $^{130}Te_2$. The Raman signal is detected as a transient loss of power on this laser with the time profile of PDA2. The relevant characteristics of the four lasers are summarized in Table I.

The two lasers within each pair are overlapped using dichroic mirrors, and each pair enters the sample cell from opposite directions, after 500 mm focal length lenses, crossing at a small angle ($<0.2°$) at a common focal region at the center of the cell. This long focal length has been chosen to minimize ac Stark broadening.[31] The focii of all lasers are similar: approximately 7 mm long (two Rayleigh ranges) and 50 μm waist diameter. The pump pair is blocked after the sample cell, while the probe pair is spectrally separated (through two Pellin–Broca prisms and a bandpass filter) and the SMA beam is spatially filtered before reaching the detector (a 1 ns rise time Si photodiode). A programmable digital delay generator controls the delay between the Q-switch and flash lamps trigger signals of both Nd^{3+}:YAG lasers, thus providing a way to perform controlled delay scans between pump and probe stages.

The coolable sample cell has been described before.[32] The overall length is 80 cm and has an inner diameter of 25 mm. This cell, which is much longer than the focal region, is preferred in order to decrease longitudinal thermal gradients across the focal volume and to avoid excessive laser irradiance on the windows. A capacitance manometer with a nominal accuracy of 0.01 mbar is permanently attached to it.

The supplied acetylene had a nominal purity of 99%. In order to remove any acetone content (used as stabilizer in the

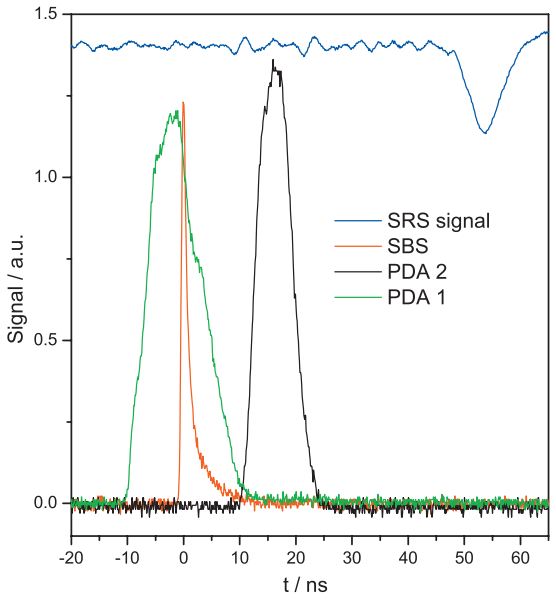

FIG. 2. Example of a typical acquisition frame showing the four traces recorded for each shot of the YAG2 laser. The SRS signal is detected as a loss superimposed to the background of the cw SMA laser. Its delay with respect to PDA2 is caused by the more distant position of the detector and the longer coax line to the oscilloscope.

cylinder), it was distilled from a sample flask held at 195 K to a liquid nitrogen cooled trap. The sample was further purified by freeze-thaw cycles before filling the cell. All measurements were made at 155 K and at a nominal pressure of 1 mbar (the actual pressure value was appropriately taken into account in the data analysis.)

B. Data acquisition

Data acquisition was done with a 2.5 GHz bandwidth digital oscilloscope. For each trigger of the YAG2 laser (firing at 30 Hz), four traces were recorded with 1000 samples (100 ps/sample) in each one: the SBS pulse, both PDA pulses and the SMA signal. Fast Si photodiodes (<1 ns rise time) were used to capture all these signals. One out of every three pulses produced by the digital delay generator is selected in order to trigger the Q-switch and the flash lamps at the 10 Hz repetition rate of YAG1 that produces the SBS pulse and pumps PDA1. Figure 2 shows an example of the signals acquired by the oscilloscope.

Both YAG1 and YAG2 exhibit a time jitter of about 2 ns peak-to-peak in the build-up time between the Q-switch trigger and the actual emission of the light pulse, and the SBS cell introduces an extra ~3 ns jitter between the incident and the reflected pulse, adding up to a combined ~5 ns peak-to-peak jitter between the pump and the probe pulses. Recording all traces on the scope allows us to obtain, *a posteriori*, the actual time delay for each shot of YAG1 without having to rely on the delay programmed on the pulse generator. This nominal delay has been varied between −4 and +30 ns in 2 ns steps (525 events are recorded at each step), plus a final delay of 400 ns (where 1400 events are recorded). The ~5 ns jitter between the pump and the probe facilitates an actually uniform sampling of delays. We have defined the delay scale as the time interval between the maxima of the PDA2 pulse and that of the product of SBS and PDA1. In the postprocessing of the data, the actual delay between the pump and the probe is measured with 100 ps resolution, and each event is binned in a 1 ns grid, except for the final delay where the influence of the jitter is negligible and all events are binned in the same 400 ns bin. Recall that the pump process is driven by the 10 Hz YAG1 laser, but we trigger the scope with the 30 Hz YAG2 laser. For each SMA trace in which there is population pumping, we subtract the next one as a "background trace," effectively eliminating any signal offset together with an electromagnetic interference induced by the 30 Hz YAG2 Q-switch that leaks into the detection system. The second trace after the YAG1 shot is disregarded. Finally, on the average, each of the bins on the 1 ns time grid contains 30 events with population pumping (465 for the final delay of 400 ns). The postprocessing of the raw data has been carried out with a MATLAB program whose main tasks are identification of possibly invalid traces (infrequent events such as unseeded Nd^{3+}:YAG laser pulses or laser-induced breakdown in the SBS cell); subtraction of background frames; normalization of the signal traces by the PDA2 energy; measurement of actual delay; measurement of the SMA signal level in a 1-ns-wide gate centered at the maximum of the signal pulse (the gate has been chosen slightly larger than the rise time of the detector); and finally, binning and averaging of the signal level within each 1 ns bin.

C. Measurement procedure

In order to obtain the large volume of experimental data necessary for a determination of the rate constants in Eq. (4), the following procedure has been repeatedly applied. First the frequency difference in the pump laser pair is tuned to generate significant population pumping through a single Raman rovibrational transition in the Q-branch of the fundamental ν_2 band, $Q(J_{pumped})$. Then the frequency difference in the probe laser pair is tuned to monitor the Raman signal in another single rovibrational component of the first hot band of ν_2, $Q(J_{probed})$. Once this has been done, the frequencies of the pump and probe laser pairs are kept fixed and the delay between the pump and the probe pulses to the sample is electronically varied between −4 and 400 ns in the way described in Sec. III B. This allows the monitoring and recording of the evolution of the signal in the $v_2=1$, J_{probed} state as a function of time (and thus number of collisions).

The procedure outlined above is repeated by changing the frequency difference in the probe laser pair for all the rovibrational transitions in the hot band (all possible values of J_{probed} including the pumped state). In the end, one obtains a set of data that describes the redistribution of the population between the rotational states in $v_2=1$ when the system evolves from an initial population distribution.

This whole procedure is then systematically repeated for different values of the pumped rotational state J_{pumped}, and a whole set of data is recorded for each one of these initial rotational states. Figure 3 shows, as an example, the dataset obtained when pumping through the Q(7) line.

The measurements produced a total of nine datasets, cor-

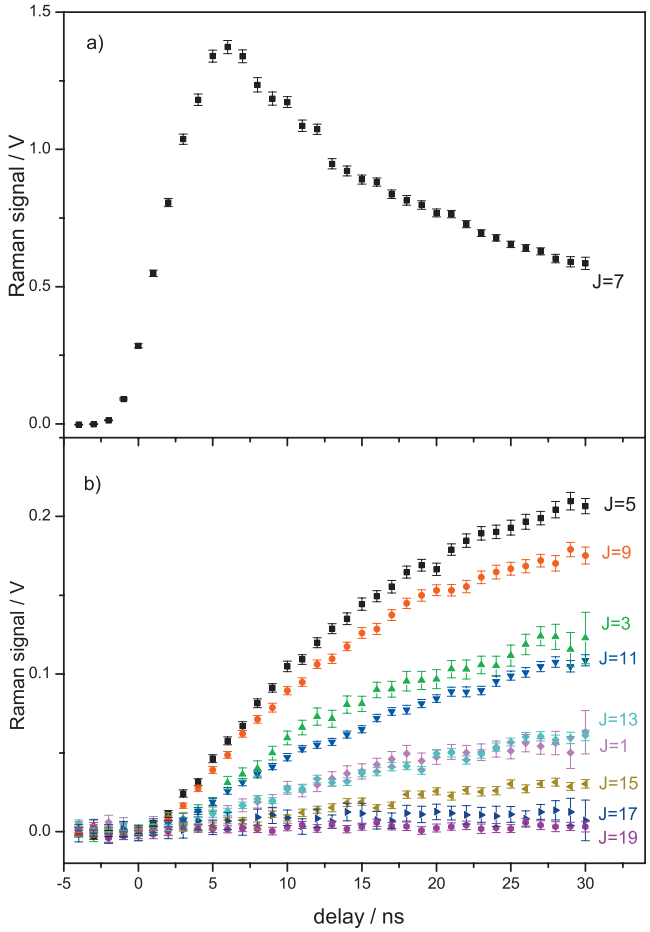

FIG. 3. Evolution of the Raman signals coming from the rotational states in v=1, J=1–19 after pumping J=7. (a) State initially populated by the pump pair (J=7). (b) Rest of states. The bars represent the error associated with the measurement expressed as $\pm 2\sigma$.

responding to the pumping of population from all the odd-J rotational states of acetylene between J=1 and J=17. Datasets with $J_{\text{pumped}}>17$ had Raman signals with a poor S/N ratio due to the small ground state population initially residing in these states at 155 K. Additionally, one extra dataset was recorded for J=15 in order to improve the poor S/N ratio obtained in the initial scans. Each one of the recorded datasets contains the evolution of the rotational population for all the observed odd-J rotational states (from J=1 to J=21) in the v_2=1 vibrational state between t=6 and t=30 ns with a 1 ns resolution. The delay of 6 ns is chosen as the shortest usable one since, as stated in Sec. III B, we must ensure that the pump process is over, and the tail of the pump SBS pulse precludes the use of delays shorter than this in the fits. (However, shorter delays up to −4 ns have been recorded in order to verify that we have a good zero baseline for the time-dependent signals.)

D. Population retrieval

The next step is the retrieval of relative populations from the experimental signals, which is a procedure repeated independently for each set of time-dependent signals *with the same pump conditions* (i.e., pumped J, cell pressure, and optics alignment). Since the frequency of the lasers is kept fixed at the center frequency of both pumped and probed transitions, we must make sure that there are no line shape-related effects that alter the relationship between the observed signal (proportional to the height of the spectral line arising from the probed transition) and the relative population (proportional to the area of the line) along the time scan. The combined bandwidth of the pump pair of lasers (which is dominated by the spectral shape of the SBS pulse that we have determined to be nearly Gaussian with a width of 0.016 cm^{-1}) is much larger than the transition linewidth of 0.003 cm^{-1}. (Basically, this is the Doppler width at 155 K since at 1 mbar pressure broadening is negligible, as estimated from the IR linewidth data.[33]) Therefore, we expect a line shape that is time independent and that is the same in the probed transitions and in the ground state ones since the pump process does not cause any velocity class selection. The combined bandwidth of the probe pair of lasers is 0.0026 cm^{-1}, just slightly smaller than the transition linewidth. In this case, the signal obtained at fixed frequency will be proportional to the integrated line intensity as long as there is no frequency drift. We have measured the frequency drifts of both ring dye lasers and both YAG1 and YAG2 with a 10 MHz accuracy wave meter and we estimate a combined maximum drift of 50 MHz/hr in each pair, which within the ~360 s needed for a complete time scan is much smaller than the spectral linewidth. Therefore, the internal coherence of the signal during the time scan for a given combination of J_{pumped}, J_{probed} is assured. These signals have now to be converted into relative populations. To this effect we have measured the signal at the long delay of 400 ns. In an independent experiment, we have confirmed a full rotational equilibration within the odd states of the v_2=1 level at this delay, therefore we can convert our signals in the 6–30 ns interval into relative populations by simply dividing them by the observed signal at 400 ns and multiplying by the expected relative population at equilibrium, calculated from the rotational partition function. In this way, any possible change in frequency match, alignment, lasers power, etc., among different J_{probed} time scans is compensated for since all the time-dependent signals are scaled to have the "correct" and known final relative fraction of population.

Vibrational relaxation, diffusion out of the probed volume, and decay of possible molecular alignment (anisotropy in the M_J distribution in the v_2=1 rotational states) can contribute to a decay component on the time-dependent signals unrelated to the RET, and thus not included in the master equation. With our experimental configuration we are pumping mainly through the isotropic part of the Q-branch transitions, so there is no alignment in the pumped levels that can interfere with the RET signals. Although it is possible to approximately model the vibrational relaxation (by a sum of exponential decays) and the diffusion effect (see, for example, the work of Bialkowski, King, and Stephenson[34]), we have chosen to compensate both of them by scaling the populations in all probed levels at each delay so that they add up to one. If both processes are J-independent, and if we probe all odd-J levels of v_2=1 where there is significant population, with this normalization we are forcing the total pumped population to remain constant during the time scan.

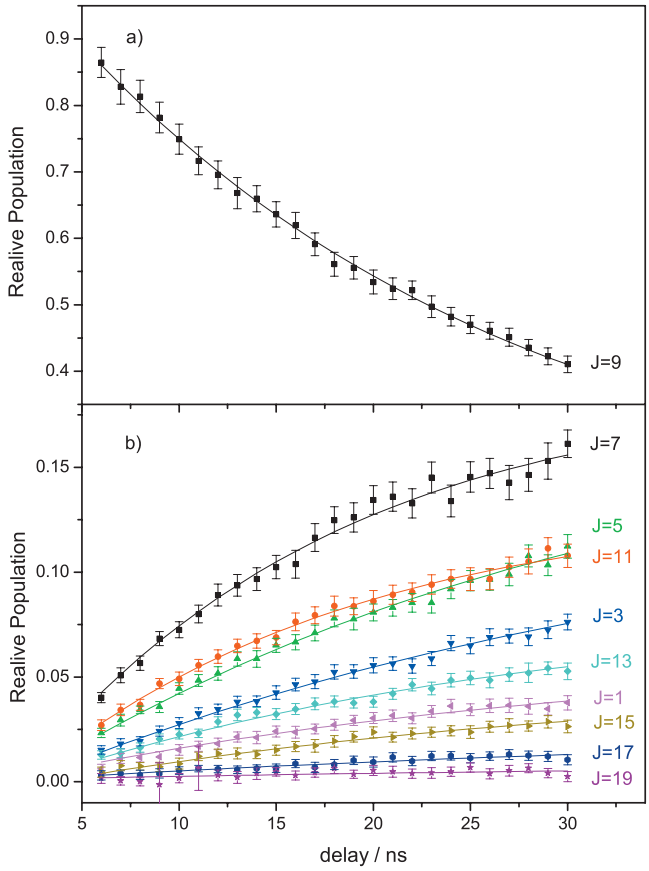

FIG. 4. Evolution of the measured (dots) and calculated (lines) fractional populations of the rotational states in $v_2=1$ up to $J=19$ after populating $J=9$. (a) State initially populated by the pump pair ($J=9$). (b) Rest of states. The bars represent the error associated with the measurement expressed as $\pm 2\sigma$.

The spectrum of $2\nu_2$-ν_2 shows no evidence of coupling with other rovibrational states[27] (so we do not expect a rotational dependence of the vibrational relaxation); diffusion has no dependence on the rotational state either, and we probe all odd rotational levels of $v_2=1$ from $J=1$ to 21, thus accounting for more than 99.6% of the *ortho*-acetylene rotational population. Therefore, our procedure is a valid approach to isolate the RET information from the time-dependent signals. An example of the population evolution retrieved for $J_{\text{pumped}}=9$ is shown in Fig. 4 along with the calculated one according to the fitting procedure described below.

E. Determination of the rate constants

The procedure above has rendered 25 points (from 6 to 30 ns) for each rotational state being monitored (all odd-J states from $J=1$ to $J=21$), so 275 data points for each pumped odd-J level (from $J=1$ to $J=17$, $J=15$ twice), totaling to 2750 data points for the whole experiment. The determination of the **k** matrix in Eq. (4) required the development of an algorithm that executed the following steps.

(1) Postulation of a trial **k** matrix. In our case it is an 11×11 matrix corresponding to all odd-J states from 1 to 21, with 55 unknowns. An initial value of 1.0 μs^{-1} $mbar^{-1}$ for all elements of the upper subtriangle of **k** proved to be adequate, with the rest of the elements calculated according to Eqs. (8) and (9).

(2) Calculation of the eigenvalues and eigenvectors of **k** that appear in Eq. (6).

(3) Calculation of the set of coefficients C_i that appear in Eq. (6). The coefficients C_i are integration constants whose values can be determined from the application of boundary conditions to Eq. (6). These integration constants are different for each of the ten recorded datasets since each one of them has been obtained by pumping population to a different rotational state. Since the **k** matrix governing the process is the same for all datasets, the algorithm has to solve Eq. (6) in parallel for each one the datasets. For each dataset, the algorithm uses the population distributions measured at all delays $t=6,7,\ldots,30$ ns, one by one, as boundary conditions, and determines a **C** vector from each one of them. All these **C** vectors are averaged to provide the final coefficients that are used in Eq. (6) for that particular data set. By operating in this way, all the collected experimental data are used in the determination of these coefficients, and the impact of experimental deviations or noise affecting any individual data point is minimized.

(4) Calculation of the populations for all the rotational states and all delays for which we have experimental measurements by simple evaluation of Eq. (6) for each data set. This renders a total number of 2750 calculated populations.

(5) Calculation of the global weighted residual as $\chi^2=\Sigma_{i=1}^{N}|n_{\text{obs}}(t_i)-n_{\text{calc}}(t_i)|^2/\sigma_i^2$. Here, $n_{\text{obs}}(t_i)$ and $n_{\text{calc}}(t_i)$ are the measured and calculated normalized populations of a given rotational state at the time t_i, respectively, N is the total number of data points, and σ_i is the experimental uncertainty attributed to the measurement.

(6) Minimization of χ^2/N by a dedicated minimization algorithm. The algorithm takes the elements of the **k** matrix as input variables and searches the phase space by modifying these variables and looking for minima in χ^2/N. Each iteration of the algorithm modifies the **k** matrix, and thus requires a complete repetition of steps (2)–(6) of this list to evaluate the χ^2/N produced by the new **k** matrix. The convergence criterion is that χ^2/N does not change more than 10^{-12}. When the procedure is complete, a **k** matrix that minimizes χ^2/N is found.

IV. RESULTS

A. Direct determination of the k matrix

In the direct determination of the **k** matrix the only constraints introduced are the sum rule (that ensures the conservation of population in a closed system) and the detailed balance condition (that relates the upper and lower subtriangles of the matrix) described by Eqs. (8) and (9). A third constraint that we found useful to guide the fits was to force all off-diagonal elements of the matrix to be positive (>0.01). Note that we consider these conditions so widely accepted that in the following this fit is referred as the *un-*

constrained or *direct* fit. Table II presents the **k** matrix obtained from the direct fit of the experimental data with these conditions. The numbers in parentheses are 1 standard deviation of the corresponding rate constant calculated using standard error determination procedures.[35] Figure 4 shows an example of the experimental populations and the calculated ones using this **k** matrix when pumping the $J=9$ state. The direct fit yields $\chi^2/N=1.09$, showing that the residuals have the same magnitude as the experimental errors used as weights.

It is apparent from the estimated errors of the elements in the last three columns of the matrix, which account for transitions departing from $J_i=17$, $J_i=19$, and $J_i=21$, that these constants are largely inaccurate, and that several of them have a value of 0.01, the minimum value allowed by the constraint included in the algorithm. The unreliability in the calculated elements of the last columns of the matrix has to be attributed, as mentioned before, to the fact that each column of the matrix is determined, to a good extent, by the dataset obtained when pumping on the J state heading that column. Given the small population fraction in these states in $v=0$ (all three of them total ~3% of the ground state population in odd-J states) the signals obtained when pumping through $J=17$ have poor S/N, and we have not even been able to measure any signal when pumping through $J=19$ and $J=21$. While it is true that the detailed balance condition should help to determine the elements in those columns with the information obtained when probing in $J=17-21$ and pumping on $J=1-15$, the S/N of those experiments is again not high enough to provide the necessary information due to the small fractional population that ends up in these states. (When rotational equilibrium is reached in $v_2=1$ at 155 K, only ~3% *of the pumped molecules* are in those states.)

Given that the elements of the last rows/columns are not well determined, it could be argued that the model could have a smaller number of parameters, but since we have indeed observed signals coming from the states involved in those rows/columns (albeit with poor S/N), the model cannot ignore the fact that those states are participating in the process. Therefore, we have chosen to present the direct results of Table II. Given the highly coupled nature of the system, it is of concern how much those elements influence the rest of the matrix: qualitatively since the elements of **k** decrease with the energy gap and with the quantum number change between the states they connect, the influence of the last rows/columns in the fit of the rest of the elements becomes less and less important as we move away from the last rows/columns. We consider then reliable the values of **k** obtained for $J_i, J_f \leq 15$, while we consider the values of **k** involving $J_i, J_f = 17-21$ unreliable, and they appear italic in Table II to indicate this fact. This claim is further supported by the results described at the end of Sec. IV B.

TABLE II. State-to-state rate constants $k_{f\leftarrow i}/(\mu s^{-1}\ mbar^{-1})$ obtained from the unconstrained fit. Numbers in parentheses are the standard errors in the same units. The rows/columns with italic numbers are also results of the fit, but we do not propose them as valid constants, as explained in the text.

$k_{f\leftarrow i}$	$J=J_i$										
$J=J_f$	1	3	5	7	9	11	13	15	17	19	21
1	−41.61(2.85)	8.01(0.13)	3.70(0.08)	2.38(0.07)	1.99(0.06)	1.21(0.09)	0.60(0.14)	0.44(0.22)	*0.01(4.20)*	*0.01(7.14)*	*0.01(15.4)*
3	16.78(0.28)	−36.74(1.38)	10.25(0.09)	5.10(0.08)	3.58(0.07)	2.69(0.08)	2.28(0.13)	1.82(0.19)	*0.31(4.26)*	*0.13(7.37)*	*0.01(15.2)*
5	10.00(0.21)	13.25(0.12)	−36.22(1.19)	11.17(0.06)	5.54(0.07)	4.53(0.09)	3.42(0.13)	2.33(0.20)	*2.40(4.85)*	*0.01(8.38)*	*0.01(16.4)*
7	6.62(0.19)	6.78(0.10)	11.48(0.06)	−36.76(1.19)	10.89(0.10)	7.04(0.11)	5.24(0.19)	3.93(0.20)	*1.80(4.93)*	*0.92(8.33)*	*0.01(18.0)*
9	4.84(0.16)	4.17(0.08)	4.99(0.07)	9.53(0.09)	−34.70(1.22)	9.63(0.12)	5.82(0.16)	4.78(0.22)	*3.08(4.43)*	*2.25(7.36)*	*0.01(16.1)*
11	2.26(0.16)	2.40(0.07)	3.13(0.06)	4.73(0.08)	7.38(0.09)	−34.16(1.14)	7.96(0.15)	5.93(0.18)	*4.23(3.06)*	*1.70(5.24)*	*0.01(11.7)*
13	0.77(0.18)	1.39(0.08)	1.61(0.06)	2.40(0.09)	3.04(0.08)	5.43(0.11)	−32.01(1.78)	7.92(0.22)	*5.01(3.02)*	*0.01(6.35)*	*1.81(11.9)*
15	0.35(0.17)	0.68(0.07)	0.67(0.06)	1.10(0.06)	1.53(0.07)	2.47(0.08)	4.85(0.13)	−31.74(3.71)	*6.91(4.22)*	*2.82(8.28)*	*0.01(13.6)*
17	*0.00(1.80)*	*0.06(0.87)*	*0.38(0.77)*	*0.28(0.76)*	*0.54(0.78)*	*0.97(0.70)*	*1.69(1.02)*	*3.81(2.33)*	−27.56(12.3)	*0.44(4.97)*	*15.91(9.19)*
19	*0.00(1.53)*	*0.01(0.75)*	*0.00(0.66)*	*0.07(0.64)*	*0.20(0.65)*	*0.19(0.60)*	*0.00(1.07)*	*0.77(2.28)*	*0.22(2.48)*	−8.27(21.8)	*0.01(8.98)*
21	*0.00(1.50)*	*0.00(0.70)*	*0.00(0.59)*	*0.00(0.63)*	*0.00(0.64)*	*0.00(0.61)*	*0.14(0.91)*	*0.00(1.70)*	*3.60(2.08)*	*0.00(4.07)*	−17.81(44.1)

B. Calculation of the k matrix with fitting and scaling laws

The large number of experimental data collected has made it possible to determine a matrix of rate constants for the system under study without the use of fitting or scaling

laws. However, given that these laws have found widespread use in the determination of the rate constants, it is interesting to fit our experimental data to some common expressions (see, for example, the reviews by Brunner and Pritchard[36] or McCaffery, Proctor, and Whitaker[37]) in order to compare the rate constants emerging from these fits to those obtained without the constraints imposed by the laws.

Among the statistically based fitting laws, the exponential gap law (EGL) (Ref. 38) and its variation, the power exponential gap law (PEGL), are commonly used. The EGL can be written as

$$k_{f\leftarrow i} = K_0 \exp\left(\frac{-\alpha|\Delta E_{fi}|}{kT}\right), \quad f > i, \tag{10}$$

where $k_{f\leftarrow i}$ is the rate constant, ΔE is the energy gap between the i and f rotational states, and K_0 and α are the two fitting parameters of the law. The PEGL (Ref. 39) is a combination of the EGL and a power law of the form

$$k_{f\leftarrow i} = K_0\left(\frac{|\Delta E_{fi}|}{B_v}\right)^{-\beta} \exp\left(\frac{-\alpha|\Delta E_{fi}|}{kT}\right), \quad f > i, \tag{11}$$

where B_v is the rotational constant of the molecule in the v vibrational state, β is an additional fitting parameter of the PEGL law, and the other symbols have the same meaning as in Eq. (10).

Dynamically based scaling laws calculate the set of rate constants by defining an initial set that constitutes the basis. Combinations of the elements of this basis set, properly scaled according to the energy and angular momentum of the different states involved in a transition, are then used to calculate the rate constant for that transition. Among the most commonly used scaling laws are the infinite order sudden (IOS) approximation[40] and the energy-corrected sudden (ECS) approximation.[41] The IOS rate constants can be calculated with the expression

$$k_{f\leftarrow i} = (2J_f+1)\exp\left(\frac{E_i - E_{\max(i,f)}}{kT}\right) \times \sum_{\Delta J}\begin{pmatrix} J_i & J_f & \Delta J \\ 0 & 0 & 0 \end{pmatrix}^2 (2\Delta J+1)k_{\Delta J\rightarrow 0}, \tag{12}$$

while the ECS law uses the more elaborate equation

$$k_{f\leftarrow i} = (2J_f+1)\exp\left(\frac{E_i - E_{\max(i,f)}}{kT}\right) \times \sum_{\Delta J}\begin{pmatrix} J_i & J_f & \Delta J \\ 0 & 0 & 0 \end{pmatrix}^2 A(J_i,J_f,\Delta J)^2(2\Delta J+1)k_{\Delta J\rightarrow 0} \tag{13}$$

In both these equations, J_i and J_f are the initial and final rotational states of the transition, respectively, $\begin{pmatrix} \cdots \\ 0\ 0\ 0 \end{pmatrix}$ is a Wigner 3-J symbol, and $k_{\Delta J\rightarrow 0}$ are the basis rate constants. The summations run over all the possible values of ΔJ, which are all the possible combinations of the two angular momentum quantum numbers J_i and J_f. ΔJ also appears in the Wigner 3-J symbols. The additional parameter in the ECS law is the adiabaticity factor A given by

TABLE III. Parameters obtained from the fits to the different rate laws expressed in Eqs. (10)–(13). Standard deviation is shown in parentheses in units of the last significant digit. χ^2/N allows for comparison of the overall quality of the fits. The direct fit of the data yields $\chi^2/N=1.09$.

Law	Parameters	χ^2/N
EGL	$K_0=16.68(9)$ μs^{-1} mbar^{-1}, $\alpha=1.589(9)$	2.69
PEGL	$K_0=41(1)$ μs^{-1} mbar^{-1}, $\alpha=1.08(2)$, $\beta=0.32(1)$	2.06
IOS-P	$a=13.5(3)$ μs^{-1} mbar^{-1}, γ 0.782(6)	4.37
ECS-P	$a=20.8(3)$ μs^{-1} mbar^{-1}, $\gamma=0.854(3)$, $R_C=2.27(7)\times 10^{-10}$ m	1.96

$$A(J_i,J_f,\Delta J) = \frac{6+[\Omega(\Delta J)R_c/2v_R]^2}{6+[\Omega(J_i)R_c/2v_R]^2}, \tag{14}$$

where v_R is the average thermal velocity, $\Omega(J)$ is the energy difference between the J level and the one immediately below,[42] and R_c is an adjustable parameter with units of length and values that are normally on the order of typical collision distances. It is common to choose the basis set with a power dependence $k_{\Delta J\rightarrow 0}=a[\Delta J(\Delta J+1)]^{-\gamma}$, where a and γ are the two fitting parameters. When this power law is used to calculate the basis set and is integrated with the scaling laws above, the two scaling laws known as IOS-P and ECS-P are obtained.

In order to fit our experimental data to these laws, variations in the MATLAB code already described were developed, but the fitting parameters of the laws were used as variables in the fit instead of the elements of **k**. Table III summarizes the values obtained for these parameters when our whole set of experimental data is fitted to each one of the four laws (EG, PEG, IOS-P, and ECS-P) described above. In all the fits the laws have been used to calculate the ascending rate constants (the lower subtriangle of **k**). Their transposed elements have been calculated with the detailed balance condition.

Figure 5 displays the curves obtained for the EGL and

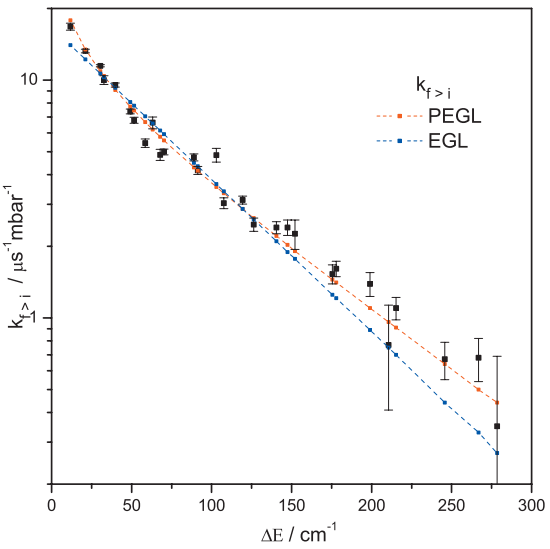

FIG. 5. Semilogarithmic plot of the EGL and PEGL fits of the experimental data. The abscissa represents the energy gap ΔE between the states connected by a rate constant. The discrete points are the ascending rate constants $k_{f\leftarrow i}(J_f>J_i)$ previously calculated through unconstrained minimization with their estimated error intervals expressed as $\pm 2\sigma$.

PEGL when the fitted parameters presented in Table III are substituted into their respective equations, together with the rate constants of the lower subtriangle of the **k** matrix calculated through unconstrained minimization (Table II) up to $J=15$.

While both fitting laws are able to reproduce how the rate constants decrease as the energy gap increases, the PEGL provides a better overall approximation to the values of the unconstrained rate constants, as shown by Fig. 5 and by the value of χ^2/N obtained from the fits: accordingly better for the PEGL ($\chi^2/N=2.06$) than for the EGL ($\chi^2/N=2.69$). The value obtained for β (0.32) is large enough to indicate a significant deviation from a pure EGL behavior in the system. This deviation and very similar β parameters have already been observed by some of the authors who studied collisional relaxation in acetylene: Pine and Looney[43] carried out IR line-broadening measurements in the $\nu_1+\nu_5$ combination band and concluded that the PEGL predicted a set of rate constants that reproduced their experimental data satisfactorily, with a $\beta=0.308$. Tobiason, Utz, and Crim[11] used a pump-probe experimental setup to study RET in $3\nu_3$ and $\nu_1+\nu_2+\nu_3+2\nu_4$ of acetylene and found a PEGL fit to reproduce their experimental rate constants better than an EGL one, with $\beta=0.320$. Conversely, the more recent work carried out by Dopheide, Cronrath, and Zacharias[14] in the ν_2 band of acetylene found the PEGL to be not as well suited as the EGL for describing the energy difference dependence in $v_2=1$. This is somewhat surprising since a better performance of the PEGL is to be expected just from a purely numerical point of view: it is an empirical variation in the EGL with an additional fitting parameter β. For $\beta=0$, the PEGL is identical to the EGL, and thus a PEGL fit should never produce worse results than an EGL fit.

The results of fitting our experimental data to the IOS-P and ECS-P dynamic scaling laws are presented in Fig. 6 for states up to $J=15$. The figure shows that the ECS-P law reproduces the behavior of the rate constants more closely than the IOS-P law. This is especially apparent for the first and last series of rate constants (those departing from $J_i=1$ and $J_i=11$), and it is confirmed by the large difference between the values of χ^2/N obtained for both fits in Table III, with that of the IOS-P fit ($\chi^2/N=4.38$) being not only more than twice the one of the ECS-P fit ($\chi^2/N=1.96$), but also much worse than those obtained for the EGL and PEGL fits. The result is not surprising given that the IOS approximation is based on the assumption of instant collisions in which the collisional geometry is frozen, thus eliminating the possibility of molecular rotation during the collision. The approximation has been shown to work well when the colliding partner does not have rotational angular momentum, as in molecule-atom collisions: for example, Heijmen and co-workers[4] used it to successfully reproduce experimental rate constants in the C_2H_2—He system and reported no improvement in the fit when the ECS-P law was used instead. For molecule-molecule collisions, however, the IOS-P law is normally found to produce worse results than the ECS-P law, which takes care of the effect of the finite collision time through the inclusion of the adiabaticity factor A in Eq. (13).

In the C_2H_2—C_2H_2 system, the better performance of

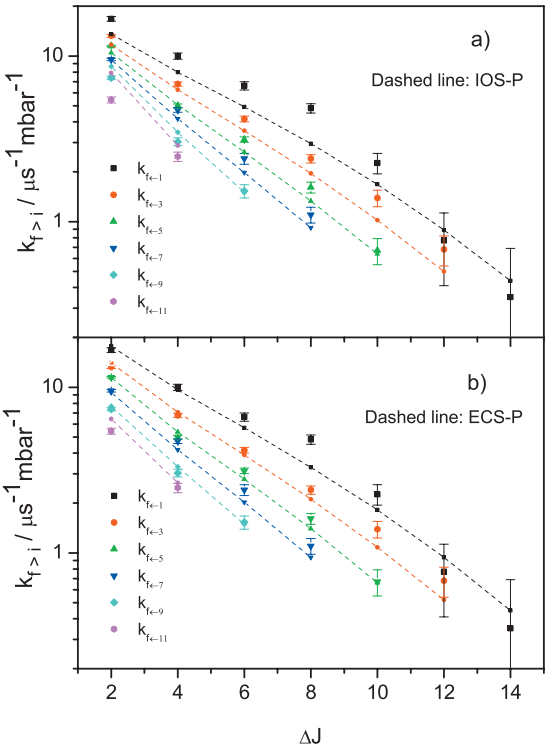

FIG. 6. Semilogarithmic plots of the IOS-P (a) and ECS-P (b) fits of the experimental data. The abscissa represents the difference in rotational quanta ΔJ between the states connected by a rate constant. The discrete points are the ascending rate constants $k_{f\leftarrow i}(J_f>J_i)$ previously calculated through unconstrained minimization with their estimated error intervals expressed as $\pm 2\sigma$.

the ECS-P law over the IOS-P has been verified in the room-temperature experiments of Dopheide, Cronrath, and Zacharias.[14] It must be mentioned, however, that while they found that the ECS-P law reproduced the experimental results much more faithfully than the IOS-P law they considered their IOS-P fit to be already satisfactory for this system, something that cannot be said in our case where the IOS-P fit is clearly the worst of the pack. The ECS-P, on the other hand, is able to reproduce the experimental rate constants better than any of the other laws across the whole range on energies studied.

The good agreement between the experimental results and the ECS-P law allows us to take the analysis of the experimental data one step further: as discussed earlier in this section, the last three columns of the **k** matrix in Table II suffer from large indeterminacy due to the nature of the experiment. In order to assess the influence of these elements in the rest of the matrix, we have fixed the rate constants of the last three columns of the upper subtriangle of the **k** matrix (corresponding to transitions departing from $J_i=17$, 19, and 21) to their calculated values according to the ECS-P law, and recalculated the **k** matrix with our minimization algorithm and this additional constraint. The number of variables in the calculation is thereby reduced from 55 to 28. Table IV shows the refined **k** matrix emerging from this fit, with the rows and columns whose values have been fixed to the ECS-P figures in italics.

It can be seen that for most of the unconstrained rate constants the change is negligible. Only those in the last free

TABLE IV. State-to-state rate constants $k_{f\leftarrow i}/(\mu s^{-1}\ mbar^{-1})$ obtained when fixing the columns $J_i=17-21$ to the values obtained with the ECS-P law fit. Numbers in parentheses are the standard errors in the same units.

$k_{f\leftarrow i}$	$J=J_i$										
$J_f=f$	1	3	5	7	9	11	13	15	17	19	21
1	−41.84(0.48)	8.01(0.12)	3.69(0.08)	2.38(0.07)	1.99(0.06)	1.19(0.08)	0.59(0.13)	0.41(0.17)	*0.47*	*0.39*	*0.33*
3	16.77(0.26)	−36.91(0.24)	10.24(0.09)	5.10(0.07)	3.58(0.06)	2.65(0.07)	2.24(0.12)	1.71(0.16)	*1.13*	*0.93*	*0.79*
5	9.99(0.21)	13.24(0.12)	−36.24(0.17)	11.16(0.05)	5.54(0.06)	4.50(0.08)	3.44(0.12)	2.29(0.16)	*1.85*	*1.52*	*1.28*
7	6.62(0.19)	6.77(0.10)	11.47(0.05)	−37.08(0.18)	10.90(0.08)	7.04(0.10)	5.28(0.17)	3.94(0.18)	*2.67*	*2.19*	*1.83*
9	4.84(0.14)	4.16(0.07)	4.99(0.06)	9.54(0.07)	−34.92(0.18)	9.60(0.10)	5.82(0.14)	4.75(0.18)	*3.65*	*2.96*	*2.45*
11	2.22(0.14)	2.36(0.07)	3.10(0.05)	4.73(0.07)	7.36(0.07)	−34.55(0.22)	7.94(0.14)	5.87(0.16)	*4.84*	*3.86*	*3.17*
13	0.76(0.16)	1.36(0.07)	1.62(0.06)	2.42(0.08)	3.04(0.07)	5.41(0.10)	−33.32(0.35)	7.73(0.19)	*6.35*	*4.95*	*4.02*
15	0.32(0.14)	0.64(0.06)	0.66(0.05)	1.10(0.05)	1.52(0.06)	2.45(0.07)	4.73(0.12)	−33.79(0.46)	*8.57*	*6.31*	*5.03*
17	*0.20*	*0.23*	*0.29*	*0.41*	*0.64*	*1.11*	*2.14*	*4.73*	−35.06	*8.23*	*6.26*
19	*0.08*	*0.10*	*0.12*	*0.17*	*0.26*	*0.44*	*0.83*	*1.74*	*4.11*	−34.95	*7.93*
21	*0.03*	*0.04*	*0.05*	*0.06*	*0.10*	*0.16*	*0.31*	*0.63*	*1.42*	*3.59*	−33.10

column ($J_i=15$) of the matrix seem significantly affected, and even for them the change is generally smaller than 5% of the original value. The diagonal elements experience somewhat larger changes since they are calculated as the sum of all the rate constants in each column. In the direct fit, many of the constants in the three lowest rows converge to the smallest values allowed by the algorithm, while in this refined **k** matrix these elements have been fixed to their (no longer negligible) ECS-derived values. In any case, the fact that the unconstrained elements change so little indicates that the quantity and quality of the data are high enough so that the elements with $J_i, J_f \leq 15$ are quite well determined, and numerical manipulations do not change their values much. Even assuming that the ECS-calculated rates imposed to the last three columns are not accurate, they are certainly a better approximation to their "true" values than the original figures. Thus, we feel confident that these elements in the refined **k** matrix of Table IV constitute a better estimation of the state-to-state rate constants than those in the original **k** matrix of Table II.

It is interesting to compare the global depopulation rates with the Lennard-Jones collision rate. This can be calculated[44] as $k_{LJ}=\sqrt{8\pi k_B T/\mu}d^2\Omega^{(2,2)^*}$ (with dimensions L^3T^{-1}), where μ is the reduced mass, d is the Lennard-Jones molecular diameter (for acetylene 42.2 nm), $\Omega^{(2,2)^*}$ is the reduced collision integral, and the other symbols have their usual meanings. At 155 K, for acetylene, $k_{LJ}=22.7\ \mu s^{-1}\ mbar^{-1}$, so our measured total rotationally inelastic collision rates are 1.4–1.8 times higher than k_{LJ}. These efficiencies, rather high for a nondipolar molecule, have already been observed by other authors (see, for example, Ref. 14 or Ref. 45) and highlight the role of long-range quadrupole forces in rotationally inelastic collisions in acetylene.

V. SUMMARY

The main result presented in this work is a new experimental setup for the determination of rotational state-to-state collisional energy transfer rates. The sequential combination of two stimulated Raman processes allows selective population of a single rotational state in the first excited state of a molecular vibration followed, after an adjustable delay, by quantitative detection of the populations present in the different rotational states of that vibrationally excited state. To our knowledge, high resolution q-cw stimulated Raman spectroscopy has never been used before as a detection technique in time resolved pump-probe measurements. It has the advantages of high spectral resolution and a linear relationship between signal intensities and populations. By systematically changing the delay between pump and detection, the evolution of the rotational populations due to collisions can be monitored. The experiment is repeated for different initial ("pumped") states so that in the end a large body of data is collected. These data constitute an experimental description of collisional relaxation between rotational states in the molecule under study, from which the rate constants can be extracted by least-squares solution of the equations that govern the process.

The validity of this approach has been demonstrated by applying it to the molecule of *ortho*-acetylene at 155 K. A total of 2750 data points has been collected that describe the evolution, between 6 and 30 ns, of the populations in the odd-J rotational states of $v_2=1$ from $J=1$ to $J=21$ from different initially populated states. Analysis of these data with an algorithm specifically developed for this task has produced a matrix **k** of collisional rate constants for all the transitions involving odd-J states between $J=1$ and $J=21$. It must be emphasized that the retrieval algorithm does not impose any constraints on the rate constants beyond their fulfillment of the detailed balance condition and the sum rule, and it allows the determination of these rate constants from the experimental data by least-squares solution of the integrated master equation, without resorting to approximations like assuming single-collision regime or the use of fitting and scaling laws.

In order to evaluate the performance of some commonly used fitting and scaling laws for the system under study, additional fits of our experimental data have been performed to the EG, PEG, IOS-P, and ECS-P laws. We have found that both the PEG and ECS-P laws are able to satisfactorily reproduce the experimental data in the range of energy gaps under study while providing rate constants that are close to those obtained through the unconstrained calculation. The EGL and especially the IOS-P law, on the other hand, are not well suited to the task.

Since the global depopulation rates are easily related to the pressure broadening coefficients in isotropic Raman Q-branches, it is of interest to compare both types of measurements, and that will be the subject of future work.

ACKNOWLEDGMENTS

This work has been funded by the Spanish Ministry of Education and Science through research Grant No. FIS2005-02029. A.R. acknowledges CSIC for an I3P contract. R.Z.M. acknowledges CSIC for the funding provided through a PIE project. We wish to thank J. Rodríguez, M. A. Moreno, and J. M. Castillo for their skillful technical help.

[1] Y. Itikawa, S. J. Kim, Y. H. Kim, and Y. C. Minh, Adv. At., Mol., Opt. Phys. **47**, 129 (2001).
[2] J.-M. Hartmann, C. Boulet, and D. Robert, *Collisional Effects on Molecular Spectra* (Elsevier, Amsterdam, 2008).
[3] J. I. Steinfeld and R. R. Gamache, Spectrochim. Acta, Part A **54**, 65 (1998).
[4] T. G. A. Heijmen, R. Moszynski, P. E. S. Wormer, A. van der Avoird, A. D. Rudert, J. B. Halpern, J. Martin, W. B. Gao, and H. Zacharias, J. Chem. Phys. **111**, 2519 (1999).
[5] T. L. Cottrell and J. C. McCoubrey, *Molecular Energy Transfer in Gases* (Butterworths, London, 1961).
[6] A. Ramos, G. Tejeda, J. M. Fernandez, and S. Montero, Phys. Rev. A **66**, 022702 (2002).
[7] A. Schiffman and D. W. Chandler, Int. Rev. Phys. Chem. **14**, 371 (1995).
[8] J. Häger, W. Krieger, T. Ruegg, and H. Walther, J. Chem. Phys. **72**, 4286 (1980).
[9] I. W. M. Smith and J. F. Warr, Chem. Phys. Lett. **173**, 70 (1990).
[10] C. P. Bewick, J. G. Haub, R. G. Hynes, J. F. Martins, and B. J. Orr, J. Chem. Phys. **88**, 6350 (1988).
[11] J. D. Tobiason, A. L. Utz, and F. F. Crim, J. Chem. Phys. **97**, 7437 (1992).
[12] S. P. Phipps, C. S. Tony, D. H. Gordon, C. H. Michael, J. K. McIver, and W. G. Rudolph, J. Chem. Phys. **116**, 9281 (2002).
[13] F. Menard-Bourcin, L. Doyennette, J. Menard, and C. Boursier, J. Phys. Chem. A **104**, 5444 (2000).
[14] R. Dopheide, W. Cronrath, and H. Zacharias, J. Chem. Phys. **101**, 5804 (1994).
[15] G. O. Sitz and R. L. Farrow, J. Chem. Phys. **93**, 7883 (1990).
[16] B. L. Chadwick, D. A. King, L. Berzins, and B. J. Orr, J. Chem. Phys. **91**, 7994 (1989).
[17] M. H. Kabir, I. O. Antonov, and M. C. Heaven, J. Chem. Phys. **130**, 074305 (2009).
[18] F. Temps, S. Halle, P. H. Vaccaro, R. W. Field, and J. L. Kinsey, J. Chem. Phys. **87**, 1895 (1987).
[19] B. L. Chadwick and B. J. Orr, J. Chem. Phys. **97**, 3007 (1992).
[20] R. L. Farrow and D. W. Chandler, J. Chem. Phys. **89**, 1994 (1988).
[21] R. S. McDowell, C. W. Patterson, and A. Owyoung, J. Chem. Phys. **72**, 1071 (1980).
[22] B. J. Orr, Int. Rev. Phys. Chem. **25**, 655 (2006).
[23] J. T. Yardley, *Introduction to Molecular Energy Transfer* (Academic, New York, 1980).
[24] R. D. Levine and R. B. Bernstein, *Molecular Reaction Dynamics and Chemical Reactivity* (Oxford University Press, New York, 1987).
[25] W. E. Boyce and R. C. DiPrima, *Elementary Differential Equations and Boundary Value Problems*, 9th ed. (Wiley, New York, 2008).
[26] E. A. Rohlfing, D. W. Chandler, and D. H. Parker, J. Chem. Phys. **87**, 5229 (1987).
[27] D. Bermejo, R. Z. Martinez, G. Di Lonardo, and L. Fusina, J. Chem. Phys. **111**, 519 (1999).
[28] G. A. Pasmanik, E. I. Shklovsky, and A. A. Shilov, in *Phase Conjugate Laser Optics*, edited by A. Brignon and J.-P. Huignard (Wiley, Hoboken, NJ, 2004), p. 223.
[29] D. Neshev, I. Velchev, W. A. Majewski, W. Hogervorst, and W. Ubachs, Appl. Phys. B: Lasers Opt. **68**, 671 (1999).
[30] R. W. Boyd, *Nonlinear Optics* (Academic, San Diego, 2003).
[31] J. Santos, P. Cancio, J. L. Domenech, J. Rodriguez, and D. Bermejo, Laser Chem. **12**, 53 (1992).
[32] F. Thibault, B. Corretja, A. Viel, D. Bermejo, R. Z. Martinez, and B. Bussery-Honvault, Phys. Chem. Chem. Phys. **10**, 5419 (2008).
[33] D. Jacquemart, J. Y. Mandin, V. Dana, L. Regalia-Jarlot, X. Thomas, and P. Von der Heyden, J. Quant. Spectrosc. Radiat. Transf. **75**, 397 (2002).
[34] S. E. Bialkowski, D. S. King, and J. C. Stephenson, J. Chem. Phys. **72**, 1156 (1980).
[35] A. A. Clifford, *Multivariate Error Analysis: A Handbook of Error Propagation and Calculation in Many-Parameter Systems* (Applied Science, London, 1973).
[36] T. A. Brunner and D. Pritchard, Adv. Chem. Phys. **50**, 589 (1982).
[37] A. J. McCaffery, M. J. Proctor, and B. J. Whitaker, Annu. Rev. Phys. Chem. **37**, 223 (1986).
[38] J. C. Polanyi and K. B. Woodall, J. Chem. Phys. **56**, 1563 (1972).
[39] S. L. Dexheimer, M. Durand, T. A. Brunner, and D. E. Pritchard, J. Chem. Phys. **76**, 4996 (1982).
[40] R. Goldflam, S. Green, and D. J. Kouri, J. Chem. Phys. **67**, 4149 (1977).
[41] A. E. DePristo, S. D. Augustin, R. Ramaswamy, and H. Rabitz, J. Chem. Phys. **71**, 850 (1979).
[42] G. Millot, J. Chem. Phys. **93**, 8001 (1990).
[43] A. S. Pine and J. P. Looney, J. Chem. Phys. **93**, 6942 (1990).
[44] J. O. Hirschfelder, C. F. Curtiss, and R. B. Bird, *Molecular Theory of Gases and Liquids* (Wiley, New York, 1964).
[45] B. L. Chadwick, A. P. Milce, and B. J. Orr, Can. J. Phys. **72**, 939 (1994).